JARQ 44 (3), 291−299 (2010) http://www.jircas.affrc.go.jp

Radioactivity Prospecting for Groundwater Development and a New Prospecting Device with a Plastic Scintillator

Masayuki IMAIZUMI[1*], Takeo TSUCHIHARA[2], Shuhei YOSHIMOTO[2], Satoshi ISHIDA[2], Sadayuki UCHIYAMA[3] and Youichi YUUKI[4]

[1] Department of Rural-Environment, National Institute for Rural Engineering, National Agriculture and Food Research Organization (NARO) (Tsukuba, Ibaraki 305−8609, Japan)

[2] Department of Rural Technologies, National Institute for Rural Engineering, NARO (Tsukuba, Ibaraki 305−8609, Japan)

[3] Clear-Pulse Co. Ltd., (Ota, Tokyo 143−0024, Japan)

[4] OYO Corporation (Kita, Saitama 331−8688, Japan)

Abstract

A large amount of undeveloped groundwater may still be left in fractured rocks of rocky mountainous areas. Points with high potential for groundwater development may be found near fault zones. The indexes ^{214}Bi and ^{214}Bi/^{208}Tl, measured by γ-ray radioactivity prospecting, are useful for detecting buried faults. We developed a radioactivity prospecting device with a three-layered plastic scintillator (PS) detector. This device is lighter weight, easier to use, and less expensive than conventional NaI detectors. A simple method for discriminating γ-rays of ^{137}Cs, ^{40}K, ^{214}Bi, and ^{208}Tl on a spectrum is proposed. We performed experiments that showed that the PS can be used for radioactivity prospecting.

Discipline: Irrigation, drainage and reclamation

Additional key words: buried fault zones, Compton edge, fracture, groundwater resources, γ-rays

Introduction

The World Water Council displays a water stress map of the world on its Website[8]. Water stress results from an imbalance between water use and water resources. According to the map, many high stress areas are in Asia and Africa. Water will be a major constraint on agriculture in coming decades, particularly in Asia and Africa[6]. Therefore, groundwater resources should be developed, preferably without any negative effects on the environment.

A large amount of undeveloped groundwater may still be left in the rocky mountainous areas of Asia and Africa. However, these groundwater resources are unevenly distributed around buried fault zones. Prospecting methods that accurately locate buried fault zones suitable for the development of groundwater resources in rocky mountainous regions are thus needed. Although aerial radioactivity prospecting by means of Gamma (γ)-ray spectrometry is generally used for monitoring the accidental release of nuclides from a nuclear facility and in uranium ore mining[7], it is also used as a geophysical radioactivity prospecting method that can be used to detect buried fault zones. This method has been successfully used as an important tool in Japan during the past ten years, but there are still several problems to solve. In particular, the detection of buried faults by radioactivity prospecting must be demonstrated empirically, and an inexpensive, highly efficient detector needs to be developed.

Detecting Buried Faults by Radioactivity Prospecting

1. Characteristics of fractures around faults

In fractured rocks, fluid flow occurs primarily via the interconnected discontinuities, whereas the blocks of solid rock are considered impermeable. Water-filled fractures are fissures-joints or bedding planes. Joints are fractures in rocks that can be caused by both tensional

* Corresponding author: e-mail imaizuma@affrc.go.jp

Received 19 December 2008; accepted 14 December 2009.

and shear stresses, and they tend to be densely distributed around fault zones.

A fault zone, which is generally shown as a geometrical plane on geological maps, actually consists of two subzones, formed by crushing and friction during fault movement: an argillization zone consisting of fault clay or gouge and a brecciated zone, consisting of fault breccias (Fig. 1). Within the fault zone, the main constituent minerals of the host rock, including feldspar and quartz, are not typically found; instead, newly formed clay minerals such as montmorillonite occur there. Fracture density is highest just outside the fault zone, and gradually decreases with distance from the fault zone.

2. Groundwater in fractured rocks around the fault zone

Engineering geologists classify rock masses according to their degree of weathering and the presence of fractures. In Japan, rock masses are divided into four classes, A to D, on the basis of three properties: weathering, hardness, and fracture density[4]. Classes A and B comprise hard rocks with minor fractures. Class C rocks are of intermediate hardness. This class is subdivided into subclasses C_H, C_M and C_L, in order of increasing the three properties. Class D rocks are characterized by remarkable softness and an absence of cohesion between exfoliation planes where clay filler is present; such rocks are easily broken by small shocks. Class D is subdivided into subclasses D_H and D_L, with the latter characterized by stronger argillization, if necessary.

We were able to observe an example of the relationship between rock mass classification and springs at dam site F along river M. At this site, topsoil and the riverbed gravel had been removed for construction of a rock fill dam, exposing the Mesozoic granodiorite basement rocks (Fig. 2). A plateau (elevation, 140 m above sea level) is widely distributed around the dam site. Groundwater recharged on the plateau flows via the local groundwater flow system to emerge as springs on the bottom of the river M at the dam site (Fig. 2). Eight faults, f1-f8, cross the dam site. The crush zone of these faults is 0.3-0.5 m wide, except for f1, which has a crush zone that is 0.5-2 m wide. The rock mass within the f1 crush zone is class D_L, and a belt of class D_H rock 2-5 m wide is distributed on the west side of the crush zone. Rock masses of classes C_H-C_M are distributed at distances greater than about 5 m from the f1 fault. Many springs occur along the fractures in the C_M-C_H rock mass east of the f1 fault, whereas few springs occur in the D rock mass. The flow rate of groundwater from individual springs is several liters per minute, suggesting a high potential for groundwater development near the fault zone.

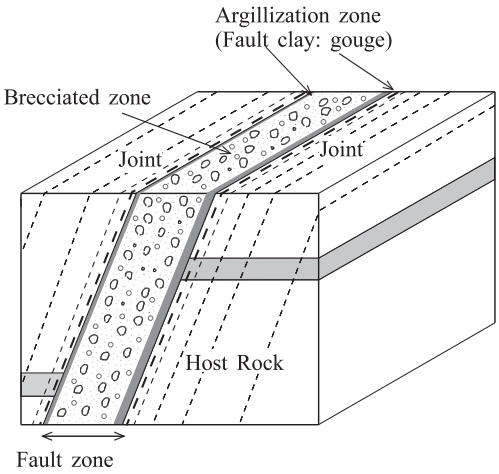

Fig. 1. Schematic fault zones

3. Role of radioactivity prospecting in groundwater investigations

Groundwater investigations in mountainous areas are carried out with the following steps.

Step 1: Initial data collection and aerial photo interpretation.

Step 2: Reconnaissance geological survey and preliminary geophysical prospecting to roughly identify fault locations.

Step 3: Detailed geophysical prospecting to confirm the fault location.

Radioactivity or electromagnetic prospecting is generally used at step 2. When the presence of a fault has been established, then, in step 3, seismic, electrical and electromagnetic prospecting are used to study the specific characteristics of the fault (e.g., the width of the fault zone and its direction of inclination). Radioactivity prospecting is also used as a supplementary method at this step. The location of a production well is determined by taking all results of the investigations into consideration.

4. Gamma-ray spectrometry

The isotopes uranium ^{238}U and thorium ^{232}Th decay to stable ^{206}Pb and ^{208}Pb, respectively, through intermediate daughter radioisotopes. During this process, α and β particles and γ-rays with many discrete energy levels are emitted. In the ^{238}U decay series, γ-rays with specific discrete energy levels are emitted from ^{214}Bi, and in the ^{232}Th decay series, they are emitted from ^{208}Tl. Environmental ^{40}K and the anthropogenic nuclide ^{137}Cs are also important isotopes used in geologic mapping. The

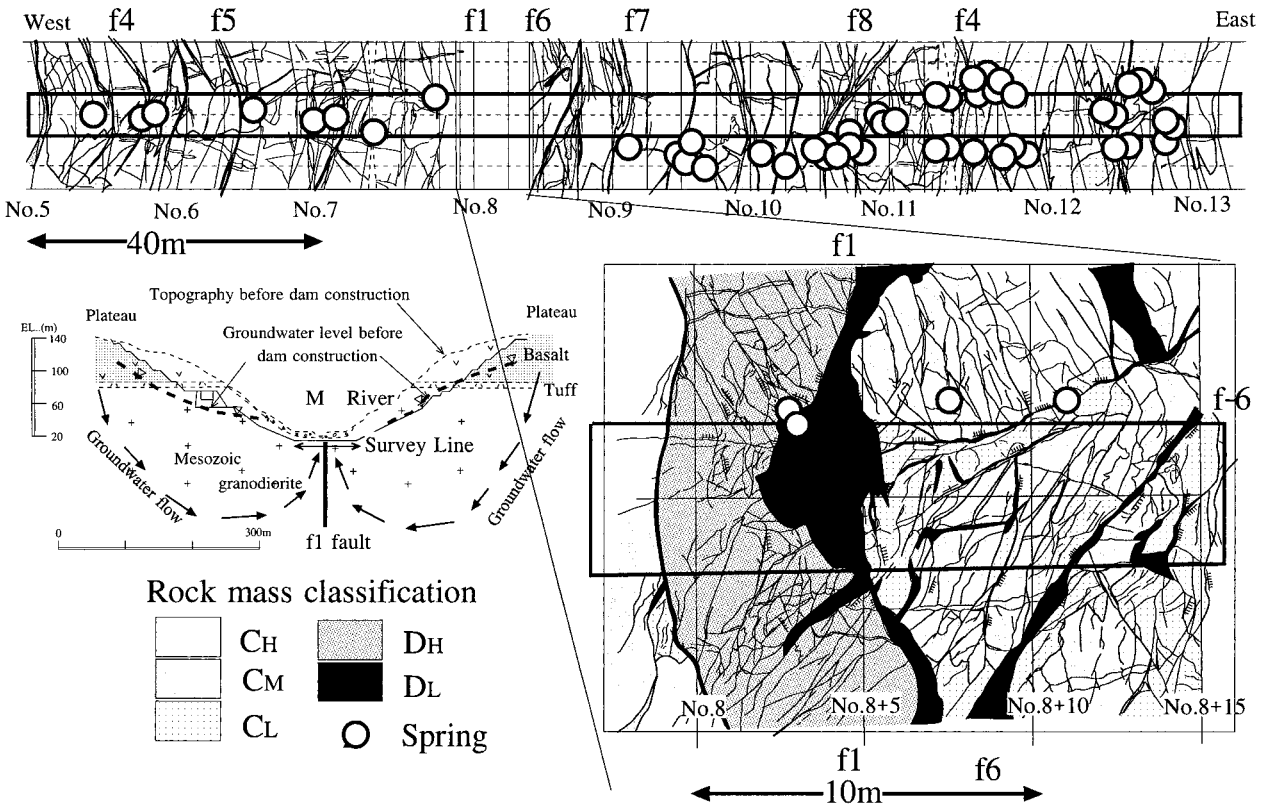

Fig. 2. Relationship between rock classification, springs and fracture lines by sketching at F dam site

amount of the parent nuclide can be measured by measuring the intensity of γ-rays discharged from the daughter nuclides at radioactive equilibrium. Thus, γ-rays from ^{214}Bi are typically measured in fault surveys to determine the amounts of ^{238}U and ^{222}Rn by a technique known as γ-ray spectrometry.

In standard practice, three quantities are measured when radioactivity prospecting is conducted with a sodium iodine (NaI) crystal detector (resolution 7%) (Fig. 3a): ^{40}K, the radioactive potassium content, measured as the integrated count between 1.37 and 1.57 MeV (the ^{40}K peak is at 1.46 MeV); ^{238}U or ^{222}Rn, the uranium or radon content, respectively, measured by the integrated count between 1.66 and 1.86 MeV (the ^{214}Bi peak is at 1.76 MeV); and ^{232}Th, the thorium content, measured by the integrated count between 2.42 and 2.81 MeV (the ^{208}Tl peak is at 2.62 MeV).

5. Detection of buried fault zones by radioactivity prospecting

Radon (^{222}Rn; 3.83-day half-life) is the only gaseous product in the uranium series. Many researchers believe that gaseous ^{222}Rn rises through the many bedrock fractures present near fault sites to the surface of the ground above the fault. Thus, the anomalous radioactivity that is frequently observed over buried faults is considered to be a direct result of the densely fractured state of the fault zone. Such faults are referred to as “opened faults”. Alternatively, other researchers believe that the radioactivity of fault sites is caused by the parent nuclides of radon, ^{238}U and radium (^{226}Ra) being absorbed and concentrated by the fault clay, because montmorillonite has a higher exchange capacity for uranium from solution, such as from groundwater, than other clay minerals[2]. Therefore, buried faults can be located by uranium radioactivity prospecting. We refer to such faults as “closed faults”.

Distinguishing between opened and closed faults is important from the viewpoint of groundwater development because opened faults may act as groundwater conduits and closed faults may act as cut-off walls. The use of radioactivity prospecting only, however, gives poor information on the fault type.

6. ^{214}Bi and ^{214}Bi/^{208}Tl as fault index

(1) Gamma-ray spectrometry of faults at dam site F

A 50-m-long survey line centering on the f1 fault (Fig. 2) was established at dam site F. A portable radio-

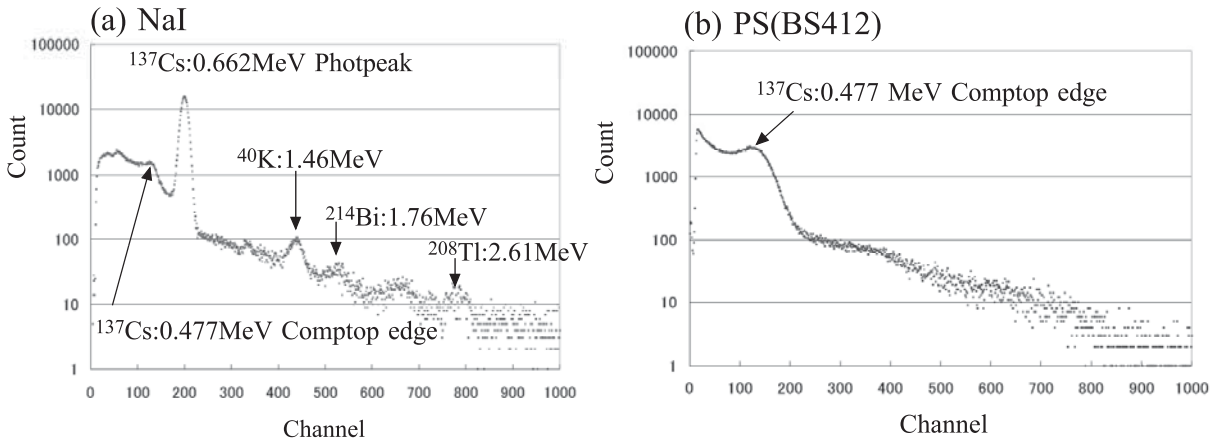

Fig. 3. Typical spectra obtained from a NaI detector (a) and from the PS of BC412 detector (b)

activity prospecting device (model 8675, Clear Pulse Co.) was used to determine the radon gas concentration emitted from the granodiorite surface at 5-m intervals along the survey line. Measuring time of the γ-ray spectrometry was 300 seconds. The radon gas concentration was determined by the activated carbon method with a PicoRad Liquid Scintillation Vial (States Accustar Labs.)[2]. Figure 4 (a) shows the fluctuations in ^{214}Bi, the ^{214}Bi/^{208}Tl ratio, and the ^{222}Rn gas concentration, and Fig. 4 (b) shows the distribution of fractures (extracted from Fig. 2). Across the main fault zone from f1 to f6, where the density of fractures is highest, ^{214}Bi and ^{214}Bi /^{208}Tl decrease rapidly to minimum values. This pattern may reflect the leaching of ^{238}U from the host rock, granodiorite. On both sides of the main fault zone, comparatively large peaks in the ^{214}Bi/^{208}Tl ratio were observed. The largest peak is about 10 m from the f1 fault on the east side (shown by the arrow). The ^{222}Rn gas concentration showed one large peak of about 3 Bq/L directly over the f1 fault. Note that the radon gas concentration peak over the f1 fault does not influence the ^{214}Bi fluctuation pattern.

(2) Gamma-ray spectrometry across already known faults

A buried fault is a fault covered by more recent deposits and soil, and such faults cannot directly be observed. Figure 5 shows the fluctuation patterns of ^{214}Bi, ^{208}Tl, ^{40}K, the ^{214}Bi/^{208}Tl ratio, and the radon gas concentration over nine, buried faults whose locations are already known[2]. ^{214}Bi and ^{214}Bi/^{208}Tl show maximum values near all nine faults. In particular, the ^{214}Bi/^{208}Tl maxima are within 0-30 m of the known fault locations. A terraced fluctuation pattern of the nuclide can be used as a faulting index, because they are expected to occur at boundaries between strata with different nuclide concentrations. Terraced changes were observed within 0-100 m from these already known faults. A ^{222}Rn gas concentration peak, determined by the activated carbon method, was detected near all faults except the Hikari fault. These peaks were within 0-180 m from the fault locations. We conclude that ^{214}Bi and ^{214}Bi/^{208}Tl peaks are useful for detecting the locations of buried faults within a tolerance error of several tens of meters.

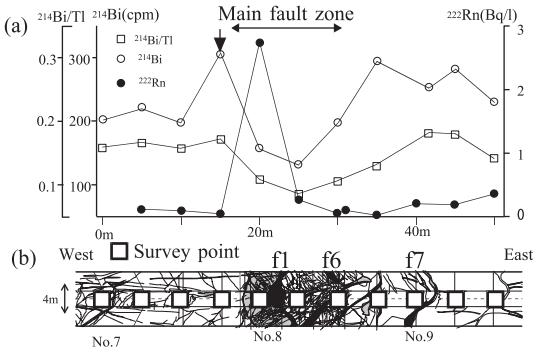

Fig. 4. Relationship between radioactivity and fractures at F dam site

Development of a New Radioactivity Prospecting Device

1. Demand for a New Detector for Radioactivity Prospecting

NaI detectors are usually used to obtain γ-ray spectrometry data for radioactivity prospecting, because they are easy to use and have been popular for the identification of unknown environmental nuclides, and methods for analyzing radioactivity prospecting data obtained with such detectors have been established[1]. Research on

	Fault Name	Geology	^{214}Bi	^{208}Tl	^{40}K	^{214}Bi/^{208}Tl	Terraced fluctuation of Nuclide	^{222}Rn	Distance between ^{222}Rn and ^{214}Bi/^{208}Tl
Active Fault	Adera Fault	Granodiorite / Granite	∩	∪	∪	∩ 20 m	×	○ 60 m	80 m
	East Abashiri Lake Faluts Group	Tertiary volcanic rocks / Tertiary volcanic rocks	∩	↘	↘	∩ 20 m	○ 100 m	○ 180 m	160 m
			∩	↘	↘	20 ∩ m	○ 0 m	○ 120 m	40 m
	Honguu Fault	Tertiary shall / Tertiary alternation	∩	∪	∪	∩ 0 m	○ 0 m	○ 10 m	10 m
			∩	∪	∪	∩	×		
None-active Fault	Tanakura East Marginal Fault	Granitic rocks / Maylonite	∪	∩	∩	∪ 0 m	○ 0 m	○ 0 m	30 m
			∩	∪	∪	∩ 30 m			
	Hikari Fault	Granodiorite / Granodiorite	∩	∪	∪	∩ 0 m	○ 40 m	×	
		Metamorphic rocks / Metamorphic rocks	∩	∪	∪	∩ 0 m	○ 0 m	×	

Fig. 5. Radioactive anomaly patterns over already known fault zones[2]
∩: Maximum, ∪: Minimum, ↘: Decease.
Figures show the distance from the location of faults.

the development of a new detector for radioactivity prospecting has focused on enlargement of the NaI crystal (density: 3.67) and reducing the overall detector weight. Increasing the crystal size would improve the accuracy of the measurement, which depends on the crystal volume. However, manufacture of a large-volume, flat NaI detector is expensive and difficult owing to the characteristics of crystal growth. Moreover, the overall weight of the detector must be reduced for use in automatic, unmanned airborne systems. Therefore, we aimed to develop a radioactivity prospecting device featuring a plastic scintillator (PS) (density of anthracene as typical PS: 1.25), which would be lighter, easier to use and less expensive than a conventional NaI detector. PSs have not been used for radioactivity prospecting because they suffer from measurement instability as well as difficulty in discerning environmental nuclides.

2. Design of a new radioactivity prospecting device

(1) Design of a detector for radioactivity prospecting

After considering many types of commercially available PSs[5], we selected BC412 (Bicron Co.) as the material for the detector from the points of view of photo-power. To discriminate between neutrons and γ-rays, the detector was designed as a three-layered structure (Fig. 6). The first PS layer (hereafter PS5) was for neutron detection, the second layer, which consisted of boron-doped paraffin, was for neutron absorption, and the third PS layer (hereafter PS50) was for γ-ray detection. The γ-rays pass through the first and second layers without any loss of energy. In contrast, most of the neutrons' energy is absorbed within the first layer. Those neutrons that pass through the first layer without being absorbed are absorbed by the second layer. Therefore, only γ-rays reach the third layer, and most of the γ-rays' energy is absorbed by the third layer.

(2) Spectral analysis with the three-layered detector[3]

If the full scale of the pulse height analyzer consists of 1,024 channels (*ch*), the net count of fast neutrons (N_{count}) present in an anthropogenic sample is calculated from the following equation:

$$N_{count} = \sum_{ch=f}^{ch=1024} E(ch) - \sum_{ch=f}^{ch=1024} BG(ch) \quad \cdots\cdots\cdots\cdots\cdots\cdots (1)$$

In this equation, f is the cut-off channel, $E(ch)$ is the gross count of each channel at the point of survey

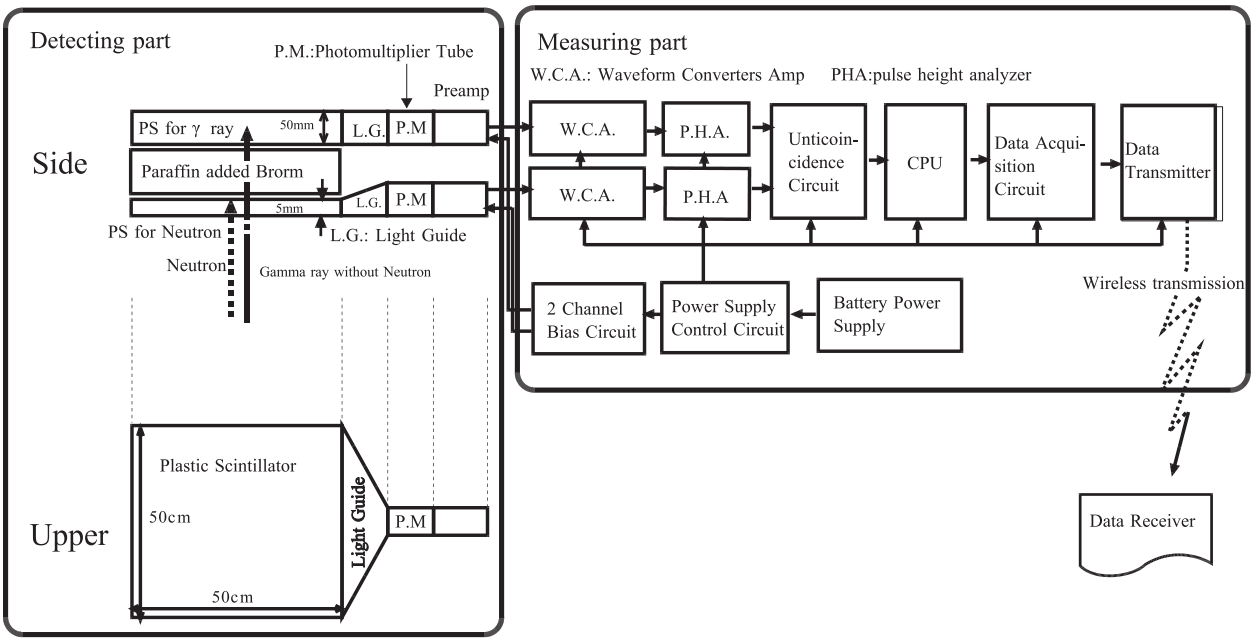

Fig. 6. Block diagram of three−layered PS detector for radioactivity prospecting

and *BG*(*ch*) is the background count of each channel (i. e., the count obtained in the absence of anthropogenic neutrons).

When γ-rays pass through the PS, they interact with the electrons and with the atomic nuclei of the PS through various mechanisms. These mechanisms, which cause the photon to lose part of its energy, can be grouped into three categories: the photoelectric effect, the Compton Effect, and electron pair production. For spectral analysis of data collected by a NaI detector, photo-peaks related to the photoelectric effect are used to discriminate the peculiar energies of each γ-emitting nuclide contained in the source (Fig. 3a). However, because the photoelectric effect does not occur within material composed of elements with low atomic numbers such as hydrogen and carbon, which are the constituent elements of the PS, photo-peaks are not observed in the spectra obtained from PS detectors (Fig. 3b). Instead, the edge of Compton scattering is used as a reference point for energy calibration in PS spectrometric measurements. However, it is difficult to identify the channel of the edge of individual nuclides in a environmental γ-ray spectrum which is a synthesis of the spectra of ^{208}Tl, ^{214}Bi, ^{40}K, and ^{137}Cs. The complexes spectrum put the individual edge out of sight. The channel of Compton edge is identified by extracting the differential curve shapes from a logarithmic spectrum at the Compton edge according to the procedure shown schematically in Fig. 7. Figure 8 shows an example of a differential curve in which the peaks correspond to the channels located at the Compton edge.

Figure 9 shows schematically the calculation method used to determine the relative intensities of ^{137}Cs, ^{40}K, ^{214}Bi, and ^{208}Tl. The spectrum of each nuclide consists of two parts: the Compton edge and the Compton plateau (Fig. 9a). The synthesized gross count of Compton scattering is separated into the net counts of each nuclide by calculations based on the locations of channels “a” through “f” in the spectrum, in accordance with the following equations:

$$^{208}\mathrm{Tl}_{count} = \left\{ \sum_{ch=b}^{ch=a} E(ch) - C(a)_{\mathrm{Tl}} \times (a-b) \right\} + \left\{ C(b)_{\mathrm{Tl}} - C(a)_{\mathrm{Tl}} \times (b-f) \right\} \quad \cdots(2)$$

$$^{214}\mathrm{Bi}_{count} = \left\{ \sum_{ch=c}^{ch=b} E(ch) - C(b)_{\mathrm{Tl}} \times (b-c) \right\} + \left\{ C(c)_{\mathrm{Bi}} - C(b)_{\mathrm{Tl}} \times (c-f) \right\} \quad \cdots(3)$$

$$^{40}\mathrm{K}_{count} = \left\{ \sum_{ch=d}^{ch=c} E(ch) - C(c)_{\mathrm{Bi}} \times (c-d) \right\} + \left\{ C(d)_{\mathrm{K}} - C(c)_{\mathrm{Bi}} \times (d-f) \right\} \quad \cdots(4)$$

$$^{137}\mathrm{Cs}_{count} = \left\{ \sum_{ch=e}^{ch=d} E(ch) - C(d)_{\mathrm{K}} \times (d-e) \right\} + \left\{ C(e)_{\mathrm{Cs}} - C(d)_{\mathrm{K}} \times (e-f) \right\} \quad \cdots(5)$$

In these equations, channels “a” through “e” are defined as the channels at the base of the Compton edge peak in the differential curve, and channel “f” is the cut-off channel (Fig. 9a). E(Ch) is the gross count. $C(a)_{\mathrm{Tl}}$ is the count of the contribution of cosmic rays at channel “a”. $C(a)_{\mathrm{Tl}} \times (a-b)$ is the count of the contribution of cosmic

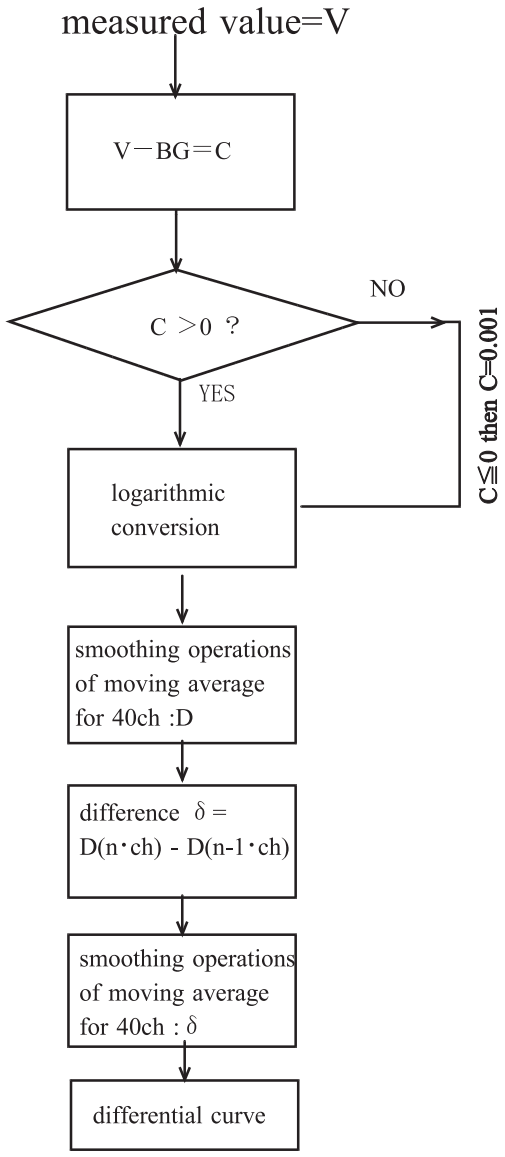

Fig. 7. Flow chart of procedure used to obtain differential curves for spectral analysis

rays to the Compton edge part of ^{208}Tl. $C(a)_{Tl}\times(b\text{-}f)$ is the count of the contribution of cosmic rays to the Compton plateau part of ^{208}Tl. The net count of the Compton scattering of ^{208}Tl is calculated by subtracting the cosmic ray contributions. Similarly, the net counts of ^{214}Bi, ^{40}K, and ^{137}Cs are calculated by subtracting the higher energy contributions.

3. Experimental

(1) Experimental setup

Experiments to test the validity of results obtained with the three-layered detector and of the analysis method were performed by using standard sources of neutrons (^{252}Cf; 0.5 MBq), γ-rays (^{137}Cs; 1.8 MBq) and potash chemical fertilizer 100kg (^{40}K; 1.6 MBq). The neutron and γ-ray sources were assumed to be point sources. The potash chemical fertilizer, which consisted of ten bags of 20 kg each, could not be treated as a point source. Figure 10(a) shows the position of the experimental device, which was suspended 3 m above the standard sources. Measurements were acquired for 5 minutes at every point.

(2) Results

Figure 10(b) is a three-dimensional (3D) diagram of the distribution of neutrons from the neutron source, measured by the PS5 layer. In this diagram, the location of the source is shown in relation to the x- and y-axes, and the distribution level of neutrons is shown on the z-axis. A conical distribution pattern was obtained. Similarly, Figs. 10(c), (d), (e), and (f) are 3D distribution diagrams for γ-rays from ^{137}Cs, ^{40}K, ^{214}Bi, and ^{208}Tl, respectively, measured by the PS50 layer from the ^{137}Cs γ-ray source. The distribution pattern of ^{137}Cs was also conical, whereas the patterns of ^{40}K, ^{214}Bi, and ^{208}Tl were flat, suggesting that these nuclides could be successfully discriminated by using equations (2) through (5). Figure 10(g) shows the distribution of ^{40}K γ-rays from the potash chemical fertilizer, which is a warped, conical pattern, reflecting the shape of the pile of ten bags of potash chemical fertilizer. These results indicate that the three-layered PS detector and the analysis method used here could accurately measure the distributions of fast neutrons and also discriminate between γ-rays from different nuclides.

Conclusion

A large amount of undeveloped groundwater may still be left in fractured rocks of rocky mountainous areas. Water-filled fractures tend to be densely distributed around fault zones. Thus, points with high potential for groundwater development are likely to be near fault zones as well. The ^{214}Bi and ^{214}Bi/^{208}Tl indexes measured by γ-ray spectrometry are useful for detecting locations of buried faults. We developed a new radioactivity prospecting device featuring a PS. This detector is lightweight, easy to use and inexpensive compared with conventional NaI detectors. Experiments showed that a three-layered PS detector and the analysis method used here could accurately measure the distributions of fast neutrons and also discriminate between γ-rays of different nuclides. These results indicate, therefore, that the PS can be used for radioactivity prospecting and that it may have a substantial advantage over the currently employed NaI detectors, although additional tests with

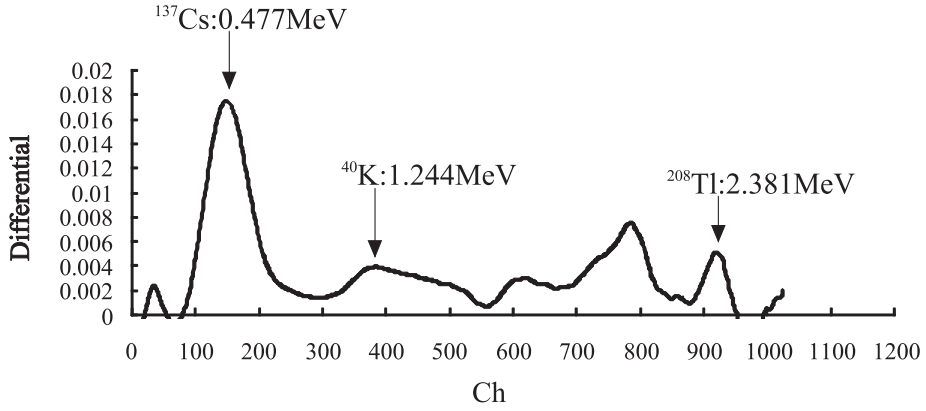

Fig. 8. Examples of differential curves obtained by means of the procedure outlined in Fig. 7

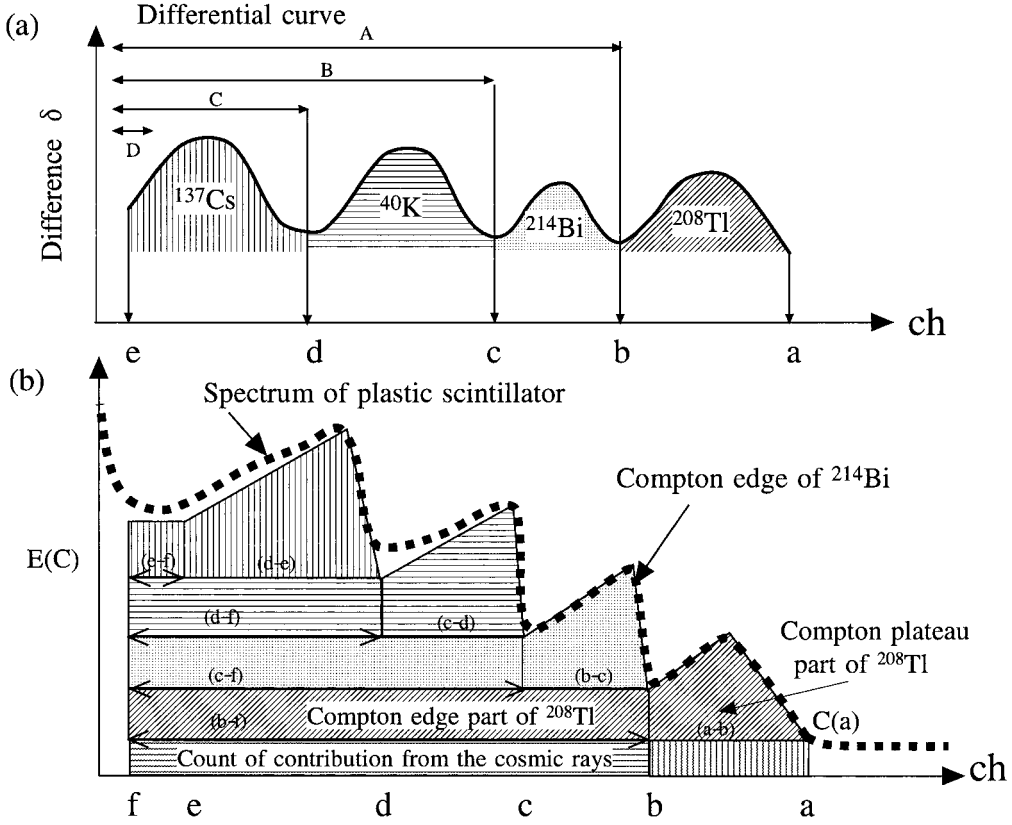

Fig. 9. Schematic figures of differential curves and PS spectrum calculated from environmental nuclides

more complex spectra are needed to more completely test the device and methodology.

Acknowledgments

This study was supported by the Budget for Nuclear Research of the Ministry of Education, Culture, Sports, Science and Technology of Japan.

References

1. Darnly, A. G (1972) Airborne gamma-ray survey techniques. *In* Uranium prospecting handbook, eds. Bowie, S. H. U., Davis, M. & Ostle, D., The Institution of Mining and Metallurgy, London, 174−211.

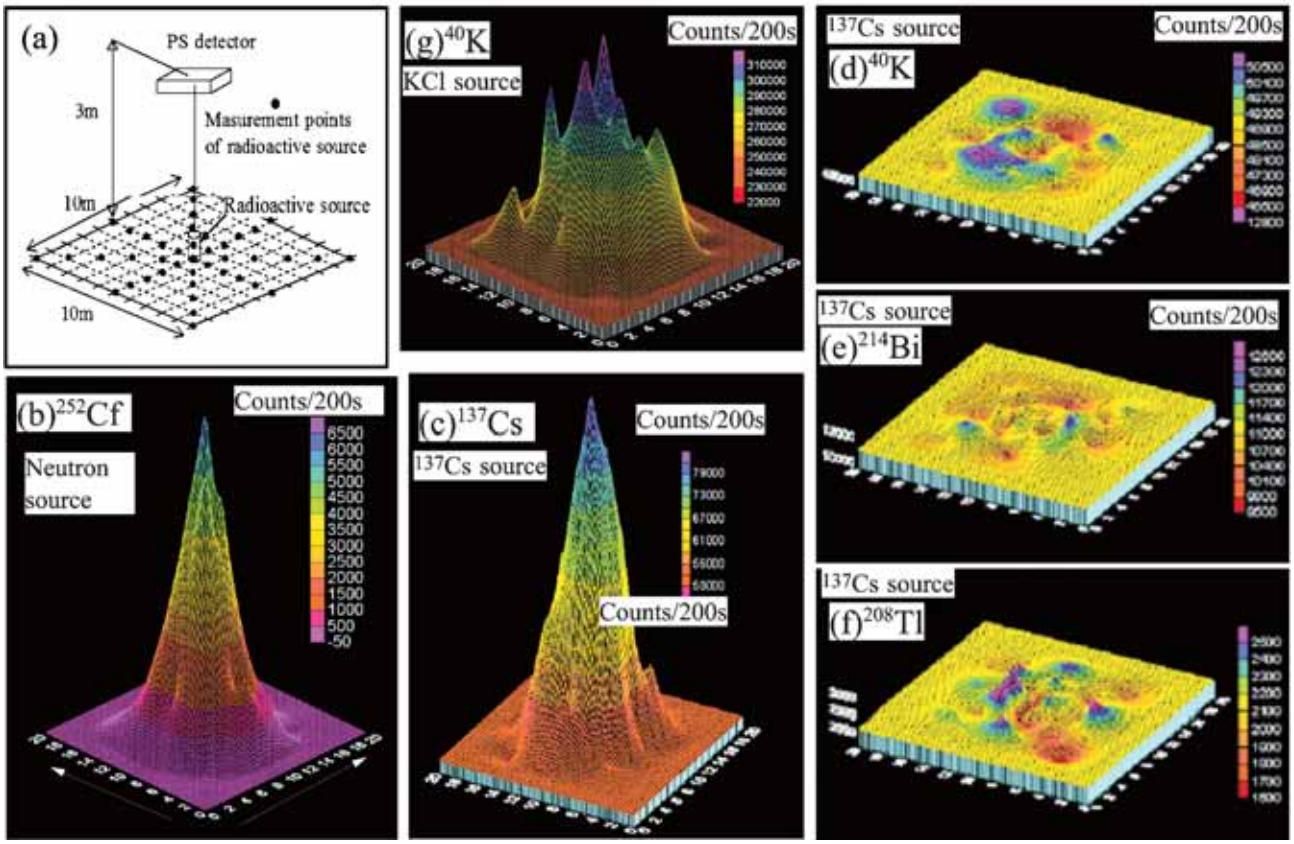

Fig. 10. Results of experiments

(a): Relationship between the detector at a height of 3 meters and standard sources of nuclide. (b): 3D distribution diagram of neutrons measured by PS5 for the ^{252}Cf neutron source. (c), (d), (e), (f): 3D distribution diagrams of ^{137}Cs, ^{40}K, ^{214}Bi, and ^{208}Tl γ-rays measured by PS50 for the ^{137}Cs γ-ray source, respectively. (g): 3D distribution diagrams of ^{40}K γ-rays measured by PS50 for the potash chemical fertilizer.

2. Imaizumi, M. (1998) Engineering geological study on discontinuous deformation in rock mass using geochemical techniques. PhD. Thesis, Chiba University, pp.204.
3. Imaizumi, M. et al. (2009) Development of radioactivity prospecting device with plastic scintillator. *Tech. Rep. National Institute for Rural Engineering*, No. **209**, 73−104 [In Japanese with English summary].
4. Japanese Geotechnical Society (2004) Method for engineering classification of rock mass, JGS:3811−2004. Japanese Geotechnical Society, Tokyo, pp.46.
5. Knoll, G. F. (2000) Radiation detection and measurement. John Wiley & Son, New York, pp.931.
6. Rijsberman,F. R. (2006) Water scarcity: Fact or fiction? *Agric. Water Manag.*, **80**, 5−22.
7. Winkelmann, I., Thomas, M. & Vogl, K. (2001) Aerial measurements on uranium ore mining, milling and processing areas in Germany. *J. Environ. Radioact*., **53**, 301−311.
8. World Water Council (2007) Water crisis. http://www.worldwatercouncil.org/index.php?id=25